

# Abelian-Higgs cosmic string evolution with multiple GPUs

J. R. C. C. Correia<sup>a,b,c</sup>, C. J. A. P. Martins<sup>a,b,\*</sup>

<sup>a</sup>*Centro de Astrofísica da Universidade do Porto, Rua das Estrelas, 4150-762 Porto, Portugal*

<sup>b</sup>*Instituto de Astrofísica e Ciências do Espaço, CAUP, Rua das Estrelas, 4150-762 Porto, Portugal*

<sup>c</sup>*Faculdade de Ciências, Universidade do Porto, Rua do Campo Alegre 687, 4169-007 Porto, Portugal*

## Abstract

Topological defects form at cosmological phase transitions by the Kibble mechanism. Cosmic strings and superstrings can lead to particularly interesting astrophysical and cosmological consequences, but this study is currently limited by the availability of accurate numerical simulations, which in turn is bottlenecked by hardware resources and computation time. Aiming to eliminate this bottleneck, in recent work we introduced and validated a GPU-accelerated evolution code for local Abelian-Higgs strings networks. While this leads to significant gains in speed, it is still limited by physical memory available on a graphical accelerator. Here we report on a further towards our main goal, by implementing and validating a multiple GPU extension of the earlier code, and further demonstrate its good scalability, both in terms of strong and weak scaling. A 8192<sup>3</sup> production run, using 4096 GPUs, runs in 40.4 minutes of wall-clock time on the Piz Daint supercomputer.

**Keywords:** cosmology: topological defects, field theory simulations, cosmic string networks, methods: numerical, methods: GPU computing

## 1. Introduction

Cosmic strings and other topological defects are a generic prediction of many theories beyond the Standard Model of particle physics, being formed by means of the Kibble mechanism (Kibble, 1976). Since the properties of these objects and their astrophysical consequences are intrinsically linked to the symmetry breaking patterns which produce them, one can think of them as fossil relics of the physical conditions in the early Universe. As such, hunting for defects in the early or recent Universe is akin to looking for evidence of specific symmetry breaking patterns. In particular a detection would indicate the presence of new physics, while a non-detection enables several constraints on theories of particle physics beyond the Standard Model. These are among the reasons why cosmic strings are a targeted for next generation cosmic microwave background (Finelli et al., 2018) and gravitational wave experiments (Binetruy et al., 2012).

These searches crucially depend on the availability of high-resolution, high-dynamic range simulations of defect networks. Unfortunately, computational constraints are already a limiting factor on these searches: it is clear that the approximations introduced to compensate for the absence of data introduce systematic uncertainties comparable to statistical uncertainties (Ade et al., 2014; Abbott et al., 2018). Using semi-analytical models with enough

degrees of freedom (Martins and Shellard, 1996; Martins, 2016) can mitigate this problem. However, the proper calibration of such models also requires high-resolution simulations. In order to alleviate this problem, one can attempt to exploit alternatives to the standard hardware architectures with the onus of optimization falling to the developers of the tool in question. The goal of this work is to describe how to optimize our previously developed GPU-accelerated cosmic string evolution code (Correia and Martins, 2020, 2019) for multiple accelerators.

Before proceeding, let us recall that there are two possible ways to simulate Abelian-Higgs cosmic string networks. In the first, one approximates the cosmic string by the action of a macroscopic (Nambu-Goto) string, which is in principle justified as long as the string effective cross-section is negligible when compared to the string length. This can be done also because the vacuum of the defect is strictly local—in the sense that fields are confined to the near-neighborhood of the string core (hence confined to a world-sheet). Simulations which assume this approximation have been done by several independent groups (Bennett and Bouchet, 1990; Allen and Shellard, 1990; Martins and Shellard, 2006; Olum and Vanchurin, 2007; Blanco-Pillado et al., 2011). The advantages of these simulations are their comparatively large dynamical range and spatial resolution; the main disadvantage is that having one a one-dimensional effective action some of the key processes affecting network dynamics (such as intercommuting and loop production) are lost and have to be enforced by hand.

In the second approach to simulating strings, one places

\*Corresponding author

Email addresses: Jose.Correia@astro.up.pt (J. R. C. C. Correia), Carlos.Martins@astro.up.pt (C. J. A. P. Martins)

fields on a co-moving discrete lattice and evolves these fields throughout cosmic time. In the strict sense of the word one does not evolve strings, but instead evolves the fields—the strings are merely specific configurations of these fields. Examples of early Abelian-Higgs simulations in the literature include Moore et al. (2002) and Bevis et al. (2007). Computational limitations imply that ordinarily these simulations can only yield more modest spatial resolutions and/or dynamic ranges, but they do have one important advantage: the microscopic field dynamics is preserved, and therefore it is relatively easy to extend the simplest Abelian-Higgs case to multiple fields (including suitable couplings). This enables the numerical study of defect types that are not described by the Nambu-Goto approximation, at least without considering additional degrees of freedom, or considering instead the Kalb-Rammond action. This flexibility is reflected in the literature: one can find examples of global defect simulations like domain walls (Martins et al., 2016), monopoles (Lopez-Eiguren et al., 2017b) and global strings (Lopez-Eiguren et al., 2017a), as well as semilocal strings (Achúcarro et al., 2014) and even hybrid networks (Hindmarsh et al., 2017b).

This second approach is the one that we adopt in the present work. Until very recently both types of string simulations exploited only one architecture: Central Processing Units, in a typical distributed computing environment. Simulations which use alternative architectures (specifically, accelerator based ones) are far more scarce. So far there have been domain wall implementations by Briggs et al. (2014) for Xeon Phi co-processors and by Correia and Martins (2017), and the more recent cosmic string implementation for GPUs by the present authors (Correia and Martins, 2020, 2019). One limitation of our GPU implementations so far pertains to the amount of physical memory available on a graphical accelerator. A way around this involves swapping parts of the lattice from host to accelerator memory constantly however, one expects this to negatively impacts performance. In what follows we address this issue by implementing and subsequently validating an extension of our previous code for multiple accelerators, and also quantify its scalability.

An outline of the rest of the paper is as follows. We start in Sect. 2 with a brief outline of our discretization procedure, and then proceed to describe its implementation for multiple GPUs in Sect. 3. Our procedure for validating the code is then described in Sect. 4, following which we discuss the tests of its scalability (both in terms of strong and weak scaling) in Sect. 5. Finally, we present some conclusions and a brief outlook in Sect. 6.

## 2. Discretization scheme

Field theory simulations of defects in cosmology rely on discretizing fields on a lattice and allow their evolution to be dictated by integrators which in the continuum limit approximate the equations of motion of the fields.

Abelian-Higgs cosmic strings arise from a Lagrangian density which is invariant under local  $U(1)$  transformations, which upon breaking of this symmetry eventually forms topological defects. We start by providing a brief overview of the aspects of the discretization process relevant for our code (and specifically for its multi-GPU extension), referring the reader to our previous work on the single GPU version (Correia and Martins, 2020, 2019) for a more detailed discussion.

The Lagrangian density has the form

$$\mathcal{L} = |D_\mu \phi|^2 - \frac{\lambda}{4}(|\phi|^2 - \sigma^2)^2 - \frac{1}{4e^2} F^{\mu\nu} F_{\mu\nu}, \quad (1)$$

where  $\phi$  is a complex scalar field, the electromagnetic field tensor is given by  $F_{\mu\nu} = \partial_\mu A_\nu - \partial_\nu A_\mu$ ,  $A_\mu$  is the gauge field (where the gauge coupling  $e$  has been absorbed),  $D_\mu \phi$  is the gauge covariant derivative given by  $D_\mu = \partial_\mu - iA_\mu$  and  $\lambda$  and  $e$  are coupling constants. Throughout this work we assume both the temporal gauge ( $A_0 = 0$ ) and a Friedmann-Lemaître-Robertson-Walker background ( $g_{\mu\nu} = a^2 \text{diag}(-1, 1, 1, 1)$ ). By standard variational principles one can obtain the equations of motion,

$$\ddot{\phi} + 2\frac{\dot{a}}{a}\dot{\phi} = D^j D_j \phi - \frac{a^2 \lambda}{2}(|\phi|^2 - \sigma^2) \quad (2)$$

$$\dot{F}_{0j} = \partial_j F_{ij} - 2a^2 e^2 \text{Im}[\phi^* D_j \phi], \quad (3)$$

along with Gauss's law,

$$\partial_i F_{0i} = 2a^2 e^2 \text{Im}[\phi^* \dot{\phi}], \quad (4)$$

where  $\dot{a}$  indicates a derivative of the scale factor with respect to conformal time.

In order to obtain the discrete form of these equations (which tell us how to update the fields at each numerical timestep) one needs to consider the principles of lattice gauge theory (Wilson, 1974) and to force both the scalar gauge couplings to scale in the following way

$$\lambda = \lambda_0 a^{2(1-s)} \quad e = e_0 a^{(1-s)} \quad (5)$$

such that the value of  $s$  can be used to either fix the co-moving width of the defect (Press et al., 1989) or to allow it to grow (for a negative  $s$ ) and subsequently shrink as expected in the true equations of motion  $s = 1$  (Bevis et al., 2007). In this way the defects are resolved and do not become smaller than the lattice spacing. With these prescriptions one obtains a discretization based on a staggered leap-frog scheme with respect to terms of second-order in time and Crank-Nicholson with respect to terms of first order in time:

$$(1 + \delta)\Pi^{x,\eta+\frac{1}{2}} = (1 - \delta)\Pi^{x,\eta-\frac{1}{2}} + \Delta\eta[D_j^- D_j^+ \phi^{x,\eta} - \frac{\lambda_0}{2} a_\eta^{2s} (|\phi^{x,\eta}|^2 - \sigma^2) \phi^{x,\eta}] \quad (6)$$

$$(1 + \omega)E_i^{x,\eta+\frac{1}{2}} = (1 - \omega)E_i^{x,\eta-\frac{1}{2}} + \Delta\eta[-\partial_i^- F_{ij} + 2e_0^2 a_\eta^{2s} \text{Im}[\phi^* D_i^+ \phi]^{x,\eta}] \quad (7)$$

$$\phi^{x,\eta+1} = \phi^{x,\eta} + \Delta \Pi^{x,\eta+\frac{1}{2}} \quad (8)$$

$$A_i^{x,\eta+1} = A_i^{x,\eta} + \Delta E_i^{x,\eta+\frac{1}{2}}, \quad (9)$$

where  $\omega = \delta(1-s)$ ,  $\delta = \frac{1}{2}\alpha \frac{d \ln a}{d \ln \eta} \frac{\Delta \eta}{\eta} = \frac{1}{2}\alpha \frac{m \Delta \eta}{(1-m)\eta}$ , and the last equality assumes cosmological power-law expansion rates with the scale factor

$$a \propto t^m \propto \eta^{m/(1-m)}, \quad (10)$$

respectively in terms of physical and conformal time. Note that  $\delta$  is responsible for the Hubble damping of the scalar field and  $\omega$  is responsible for damping the gauge field. In particular, the damping of the gauge field when  $s \neq 1$  is responsible for upholding the version of the previously stated Gauss's law to machine precision. We remark as well that all spatial derivatives are accurate to  $\mathcal{O}(\Delta x^2)$ .

In order to completely describe the communication and memory access patterns of our code, we must also describe gauge covariant-derivatives,  $D^+\phi$ , and the derivatives of the gauge field strength  $\partial^- F_{ij}$  in greater detail. In order to accurately preserve gauge invariance on the lattice these two quantities can be defined using so-called link variables,

$$U_j^x = e^{-iA_j}, \quad (11)$$

which describe the gauge fields on the lattice as parallel transporters of the scalar field  $\phi$ . With these we can properly define the modified Laplacian stencil,

$$D_j^- D_j^+ \phi^x = \sum_j \frac{1}{\Delta x^2} [U_j^x \phi^{x+k_j} - 2\phi_j^x + (U_j^{x-k_j})^* \phi^{x-k_j}], \quad (12)$$

and the spatial components of the gauge field strength can be defined with the real part of the following product of link variables,

$$\Xi_{ij} = U_j^x U_j^{x+k_j} (U_j^{x+k_i})^* (U_j^x)^* \quad (13)$$

$$= \exp[i\Delta x (\partial_i^+ A_j'(x) - \partial_j^+ A_i'(x))]. \quad (14)$$

In order to validate the code and, more generally, quantitatively describe the evolution of cosmic string networks in production runs, one must compute and output at least two key network observables: the mean string separation  $\xi$  and the mean velocity  $v^2$ . Our code can compute and output each of these variables in two separate ways. For the mean string separation these are

$$\xi_{\mathcal{L}} = \sqrt{\frac{-\mu V}{\sum_x \mathcal{L}_x}}, \quad \xi_W = \sqrt{\frac{\mathcal{V}}{\sum_{ij,x} W_{ij,x}}}. \quad (15)$$

The first one comes from Bevis et al. (2007) and is based on the Lagrangian being strongly negatively peaked at the string core while approaching zero away from the string. The second one comes from the lattice based winding from

Kajantie et al. (1998). There are also two different estimators to compute the mean squared velocity,

$$\langle v^2 \rangle_\phi = \frac{2R}{1+R}, \quad \langle v^2 \rangle_\omega = \frac{1}{2} \left( 1 + 3 \frac{\sum_x p_x \mathcal{W}_x}{\sum_x \rho_x \mathcal{W}_x} \right), \quad (16)$$

where  $R$  is the ratio,

$$R = \frac{\sum_x |\Pi|^2 \mathcal{L}}{\sum_{x,i} |D_{x,i}^+ \phi|^2 \mathcal{L}} \quad (17)$$

The first estimator is comes from Bevis and Saffin (2008) and is based on considering a boosted static string. A complete derivation can be found in Hindmarsh et al. (2017a). The second estimator is based on the equation of state parameter and has also been used in Hindmarsh et al. (2017a).

Deep in eras where the scale factor evolves according to Eq. 10 (that is, with a constant expansion rate  $m$ ), we expect these observables to exhibit scale-invariant behaviour (Martins, 2016): the string separation should grow linearly with time,  $\xi \propto \eta$ , and the mean velocity should be constant,  $v \propto \text{const}$ . Note that the proportionality factors for different expansion rates  $m$  depend on  $m$  itself and also on other parameters, in a way that is quantitatively described by the analytic velocity-dependent one-scale model (Martins and Shellard, 1996; Martins, 2016). A recent accurate calibration of this model has been presented in Correia and Martins (2019).

### 3. Extension to multiple accelerators

In order to enable taking a large lattice and dividing it among multiple accelerators, such that they can all partake in evolving the fields, we must consider that due to the modified Laplacian stencil and the derivative of the link variables, such field values ( $\phi, A$ ) must be communicated between sub-domains. In order to allow such extension to multiple nodes in a network (as is standard in most high performance computing facilities) we use the Message-Passing-Interface (MPI) to facilitate communications. Throughout this work we assume a 3D decomposition.

In the Compute Unified Device Architecture (CUDA), all code to be executed by a graphical accelerator is contained in functions denoted as kernels. In order to implement the 3D decomposition, in addition to the kernels which evolve field quantities, we add kernels that pack outer values of the core of each sub-domain into additional buffers which are then sent to neighboring sub-domains via *Isend* (from MPI). After both *Isend/Irecv* complete (a *WaitAll* barrier is necessary to ensure that all communication is complete) we use similar unpacking kernels to place the contents of received buffers into the boundaries of each sub-domain. Note that launching CUDA kernels from the host is non-blocking (relative to the host) which is why

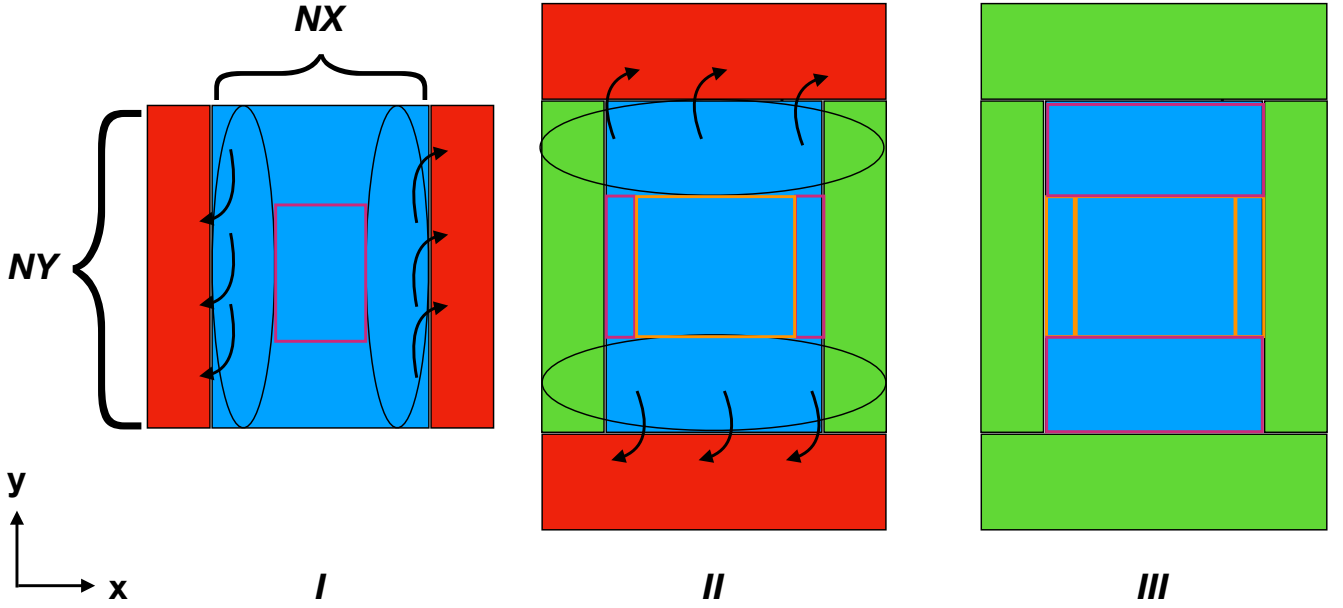


Figure 1: The packing procedure along two different directions. Blue represents the core of each domain (of size  $NX \times NY \times NZ$ ), red represents the buffers being filled with appropriate values to send to neighboring sub-domains and green represents an already received buffer. In the left panel, the buffer values come only from the blue inner core. After communication has taken place in this first direction, one can unpack the received buffer into the boundaries of the sub-domain. Once done, one can start packing the communication buffers for the next direction. This involves using not only the blue inner core but the freshly unpacked boundaries (in green). The pink boxes indicate domain areas where one updates fields  $E$  and  $\phi$  either as the packing procedure begins (left and middle panels) or after all communication has taken place (right panel) whereas orange indicates these areas have already been updated.

one must include a *CUDAStreamSynchronize*, which ensures the packing kernel and all kernels before it have completed in time, in appropriate places. Note that a CUDA Stream is a sequence of commands launched in order (in this case a sequence of kernels). In order to obtain maximal bandwidth and minimal latency the communicated buffers are allocated in Unified Memory and Remote direct memory access is allowed, as noted in standard good practices (PRACE, 2017).

Note that some key requirements must be fulfilled in order to correctly satisfy all boundary conditions. For example, due to the diagonal terms of the gauge field  $A_i$  (needed to compute the derivative of the gauge field strength) one must also pay attention to "corners". The way to correctly handle this is to use the "diagonal trick" which means the corners along a given direction come from values exchanged from the previous communication in another direction. This dependency of exchanges in one direction upon preceding exchanges implies that communication must proceed in a given specific order. In our case this means communication must proceed as follows:

1. Pack the values to be sent to neighbors along X (outer part of the inner  $NX \times NY \times NZ$  part of the domain);
2. Send packed buffers to neighboring sub-domains;
3. Unpack received values into boundaries in the X direction;

4. Pack the values from the outer cells of the inner  $NX \times NY \times NZ$  along with values received from the previous exchange (to ensure corners are appropriately handled), to be sent to neighbors in the Y direction;
5. Exchange packed buffers in the Y-direction;
6. Unpack received buffers into the boundaries of the sub-domain;
7. Pack the values from not only the inner core from the sub-domain but also from the two previous exchanges;
8. Exchange packed buffers in the Z-direction;
9. Unpack received buffers into boundaries.

Having done this one can choose to perform the update of  $E$  and  $\Pi$ . However, in order to obtain Weak scaling above 90% for thousands of GPUs one must also consider overlapping the compute and communication work. In order to compute overlap we can update the inner core of each sub-domain while one starts packing the values for communication along X. Note that the outermost cells of this inner core require values from the boundaries which are still being communicated. This means that the size of the inner core we update must be  $(NX - 2) \times (NY - 2) \times (NZ - 2)$  (while for communication it remains  $NX \times NY \times NZ$ ). After exchange in the X-direction is completed, one can begin updating the outer part of the along X (given

that the necessary boundary is not available), while communication is completed in the Y-direction. This proceeds until all boundaries are exchanged and  $E$  and  $\Pi$  are updated everywhere. At such a point, one can simply update  $\phi$  and  $A$ .

A schematic view of this is presented, for the simpler case of 2 dimensions, in Figure 1. Note that here we can also make use of multiple CUDA streams (asynchronous with respect to each other) in order to allow overlap between the compute kernels and the pack/unpack kernels (one stream per each pack/unpack kernel). This also means that the correct dependencies between streams must be enforced. This can be done using a combination of *cudaEventRecord* (which signals the completion of a kernel in a given stream) and *cudaStreamWaitEvent* (which can force a stream to wait for completion of a given event in another stream).

#### 4. Code validation

In order to verify that the simulation boxes evolved by the new code behave as expected, one must compare the numerically measured physical estimators (the slope of the time dependence of the mean string separation and the asymptotic mean velocity squared) to the values available in the literature, including those previously obtained (at different box sizes) with the single GPU version of the code, which has been previously validated (Correia and Martins, 2020). We will do this with constant co-moving width simulations in the canonical radiation and matter dominated epochs, since there are the most common in the literature.

The results of this validation test are summarized in Table 3 and also in Figures 2 and 3 (respectively for the radiation and matter dominated eras), and in a nutshell the new code is in agreement with the results in the literature, given the reported (one sigma statistical) uncertainties.

Regarding the mean string separation, our previously obtained values at  $512^3$  were in agreement with the values obtained by Bevis et al. (2007) with the same box size. The larger simulations in the current work confirm the slight drift of the scaling value of  $\xi$  to lower values, as can be seen in Bevis et al. (2010) for  $1024^3$  and Daverio et al. (2016) at  $4096^3$  (see also Hindmarsh et al. (2017a)). This slow drift may be due to the fact that a higher (spatial) resolution affects the main energy loss mechanisms for the network (loop production and scalar and gauge radiation) in slightly different ways, which in turn impacts the string network density. A detailed exploration of this hypothesis, in the context of the recently improved and calibrated velocity-dependent one scale model (Correia and Martins, 2019) is in progress. We also note that the two independent estimators for the mean string separation, defined in Eq. 15, lead to fully consistent values for  $\xi_{\mathcal{L}}$  and  $\xi_W$ .

As for the average velocity squared, our previous work (Correia and Martins, 2020, 2019) using the estimators of

Hindmarsh et al. (2017a) had already established qualitative agreement with the values in the literature, up to and including  $4096^3$  simulations. Here this agreement continues. Note that in the case of the velocities there is no statistically significant drift in the scaling value as a function of the box size. On the other hand, and in agreement both with Hindmarsh et al. (2017a) and with our earlier  $512^3$  study, our present analysis confirms that the velocity estimator based on the gradient on  $\phi$  leads to values that are consistently lower than those of the equation of state estimator, by about ten per cent at all box sizes.

#### 5. Performance

All the performance tests we report herewith were performed at Piz Daint, the largest supercomputer in Europe. At the time of the measurements, this facility contains 5704 nodes each equipped with with one NVIDIA Tesla P100. All benchmarks are performed assuming the evolution of a local string as described in the previous sections.

To closely mimic a typical use case (in other words, a typical production run), we choose to compute the Lagrangian based mean string separation and the mean velocity squared estimated from  $\phi$  and its conjugate field  $\Pi$ , weighted with the Lagrangian. The computation of these network averaged quantities occurs at every 5 time-steps. The initial conditions are generated at random in each case.

Both strong and weak scaling are arguably relevant metrics for the problem at hand, but in pragmatic terms the weak scaling is the most relevant one: often (due to computational limitations) one must extrapolate from these relatively small simulations to cosmologically relevant scales. Targeting larger and larger simulation sizes (and therefore larger dynamic ranges) would lessen this problem. In particular, doubling the box size along each dimension, besides the obvious increases in volume (by a factor of 8) and in dynamic range (by a factor of 2), also increases the range of physical scales between string thickness and horizon size that can be probed. In our case the strong scaling would only become critical if the total wall-clock times of the simulation were much larger.

For simulations of cosmic string (or other cosmological defects) simulations the dynamic range of the simulation increases with the size of the whole box, being proportional to the length of the smallest box side  $N$  (for any cubic simulation box  $N^3$ ). Given this feature of string simulations, for the weak scaling diagnostic we quantify the time taken to evolve the lattice a number of time-steps equal to the number of time-steps required to evolve the smallest simulation box we considered, which has a size of  $256^3$ . This corresponds to a total of 640 time steps.

We characterize both the weak and strong scaling using a speed-up factor,  $S$ , and a parallel efficiency,  $E$ . Both are calculated in comparison to a reference wall-clock time,  $t_{ref}$ . In strong scaling this corresponds to the wall-clock time necessary to fully evolve the full dynamic range with

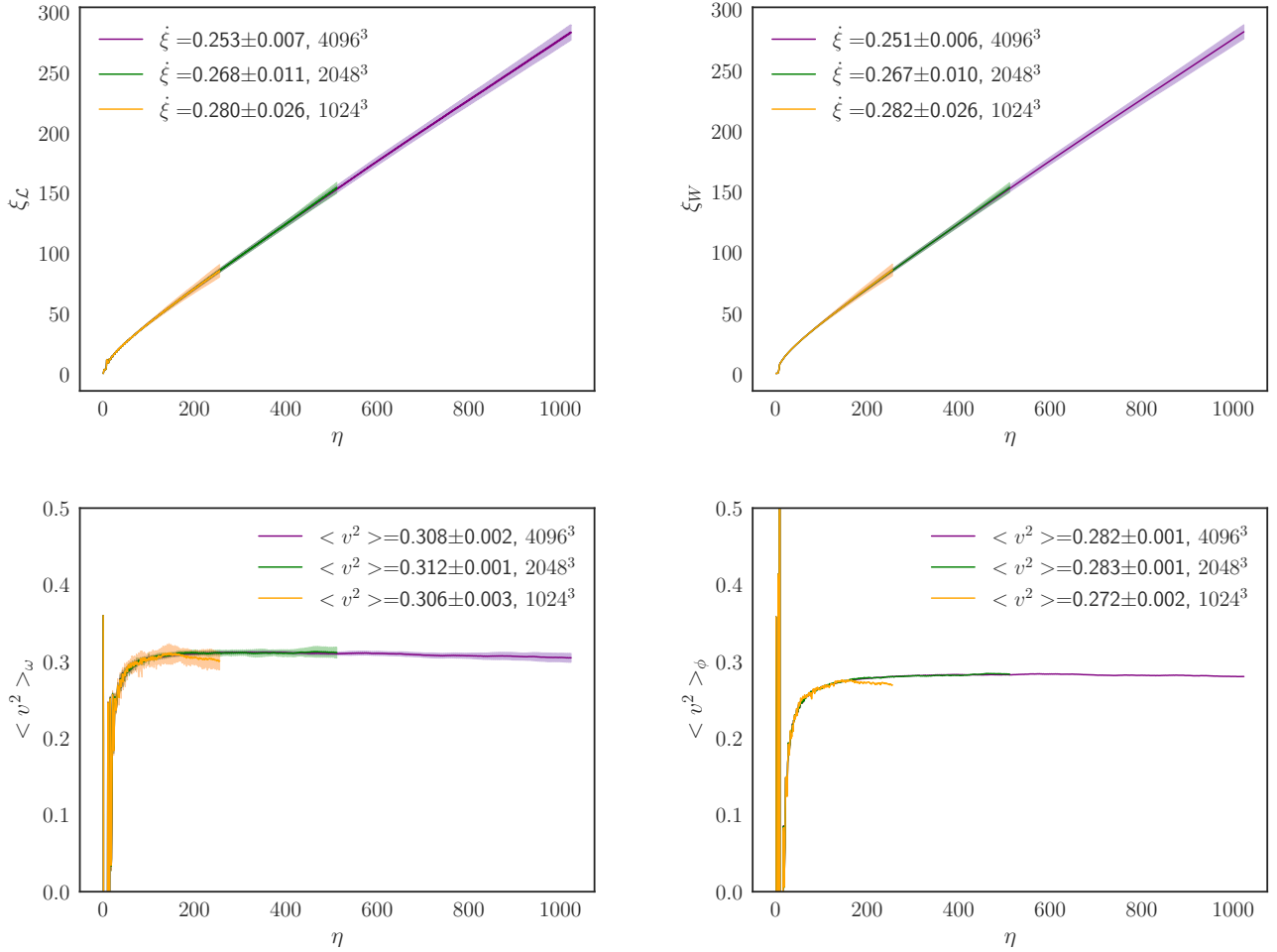


Figure 2: The evolution of the four relevant average network estimators, defined in Eqs. 15 and 16, for the average of 20 runs in the radiation-dominated epoch ( $m = 1/2$ ), with lattice sizes of  $4096^3$ ,  $2048^3$  and  $1024^3$ , using 4096, 512 and 64 GPUs respectively. We assume constant co-moving width throughout.

Size	m	$\dot{\xi}_{\mathcal{L}}$	$\dot{\xi}_W$	$\langle v^2 \rangle_{\omega}$	$\langle v^2 \rangle_{\phi}$	Reference
$4096^3$	1/2	$0.253 \pm 0.007$	$0.251 \pm 0.006$	$0.308 \pm 0.002$	$0.282 \pm 0.001$	This work
$2048^3$	1/2	$0.268 \pm 0.011$	$0.267 \pm 0.010$	$0.312 \pm 0.001$	$0.283 \pm 0.001$	This work
$1024^3$	1/2	$0.280 \pm 0.023$	$0.282 \pm 0.026$	$0.306 \pm 0.003$	$0.272 \pm 0.002$	This work
$512^3$	1/2	$0.30 \pm 0.02$	$0.32 \pm 0.03$	$0.32 \pm 0.01$	$0.31 \pm 0.01$	Correia and Martins (2020)
$512^3$	1/2	$0.31 \pm 0.02$	-	-	-	Bevis et al. (2007)
$1024^3$	1/2	-	$0.26 \pm 0.02$	-	-	Bevis et al. (2010)
$4096^3$	1/2	$0.234 \pm 0.006$	$0.244 \pm 0.005$	-	-	Daverio et al. (2016)
$4096^3$	2/3	$0.252 \pm 0.010$	$0.250 \pm 0.009$	$0.265 \pm 0.001$	$0.243 \pm 0.001$	This work
$2048^3$	2/3	$0.256 \pm 0.006$	$0.257 \pm 0.005$	$0.264 \pm 0.001$	$0.240 \pm 0.001$	This work
$1024^3$	2/3	$0.279 \pm 0.016$	$0.285 \pm 0.017$	$0.255 \pm 0.003$	$0.228 \pm 0.004$	This work
$512^3$	2/3	$0.29 \pm 0.01$	$0.29 \pm 0.02$	$0.27 \pm 0.01$	$0.25 \pm 0.01$	Correia and Martins (2020)
$512^3$	2/3	$0.30 \pm 0.01$	-	-	-	Bevis et al. (2007)
$1024^3$	2/3	-	$0.28 \pm 0.01$	-	-	Bevis et al. (2010)
$4096^3$	2/3	$0.235 \pm 0.008$	$0.247 \pm 0.008$	-	-	Daverio et al. (2016)

Table 1: The asymptotic rate of change of the mean string separation  $\xi$  and the mean velocity squared  $\langle v^2 \rangle$  for the estimators defined in the text, in the radiation and matter eras, for our simulations with box sizes of  $4096^3$ ,  $2048^3$  and  $1024^3$ , using 4096, 512 and 64 GPUs respectively. The error bars are the statistical uncertainties from averages of 20 runs with different initial conditions. For comparison we show the results reported in Correia and Martins (2020) from the single GPU code (for averages of 12  $512^3$  simulations) as well as results from simulations with CPU-based codes. The range of timesteps used for each fit to the GPU simulations is respectively  $[517, 1023.5]$ ,  $[300.5, 511.5]$ ,  $[100.5, 255.5]$ ,  $[80, 128]$  for the  $4096^3$ ,  $2048^3$ ,  $1024^3$  and  $512^3$  simulations.

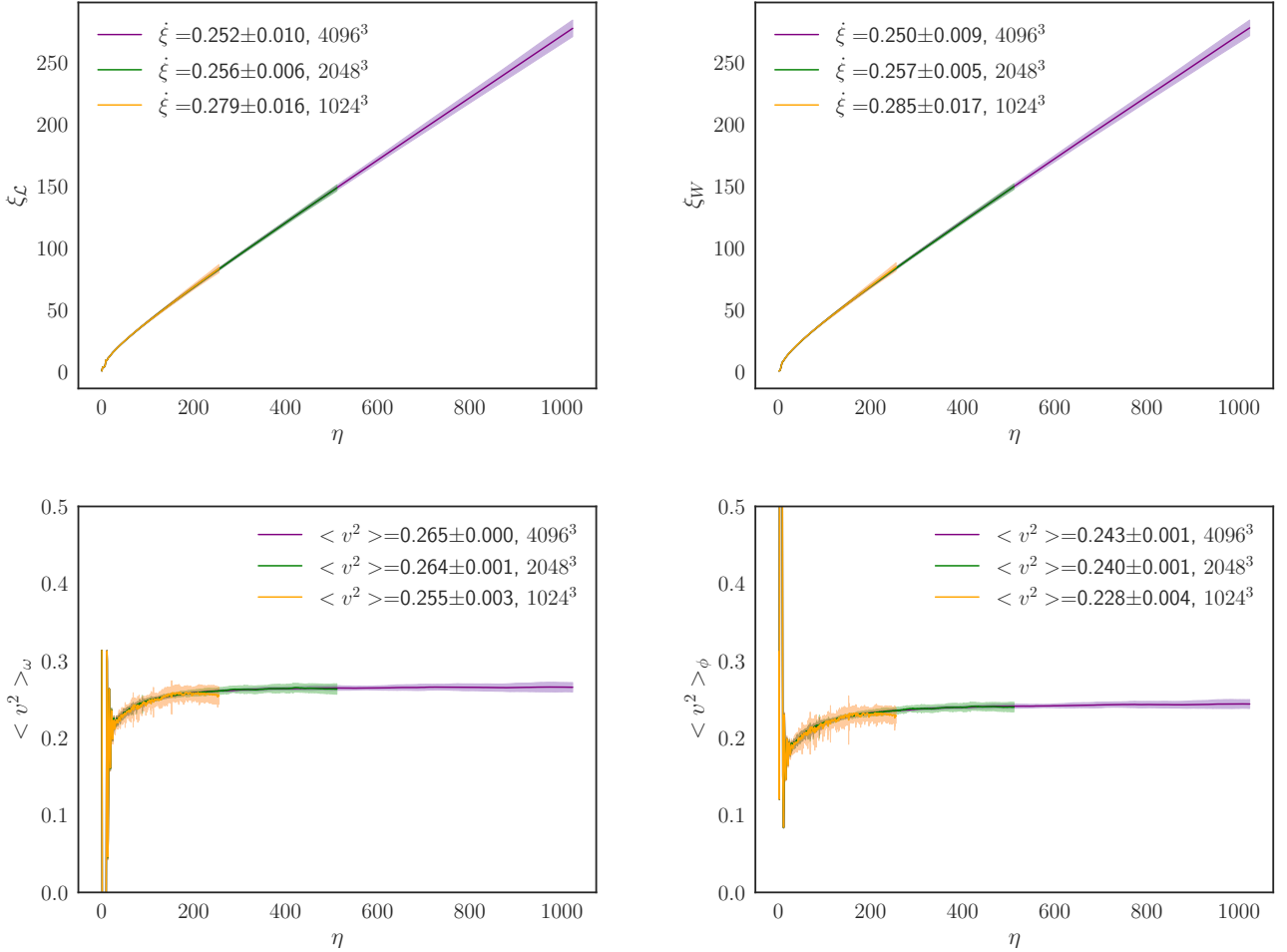


Figure 3: Same as Fig. 2, for the matter-dominated epoch ( $m = 2/3$ ).

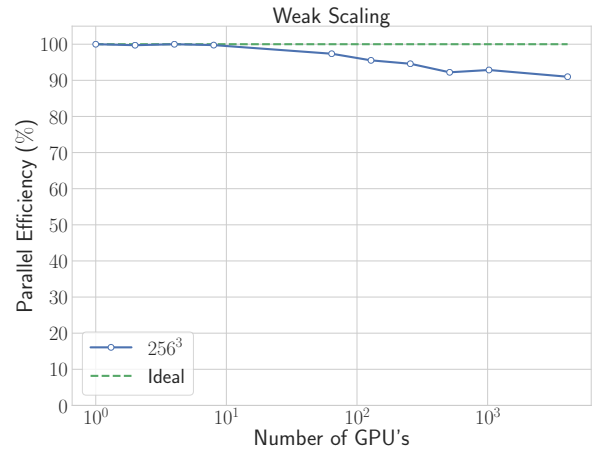
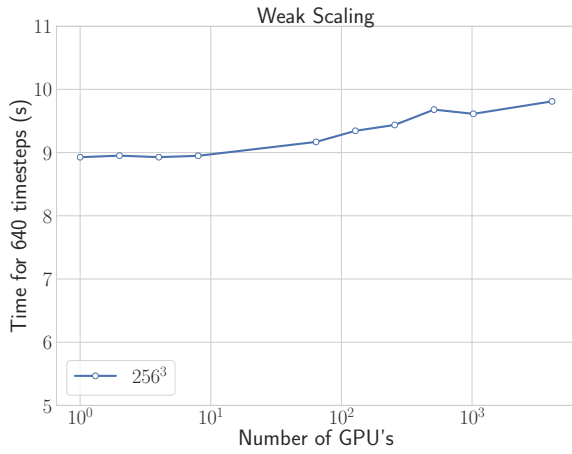
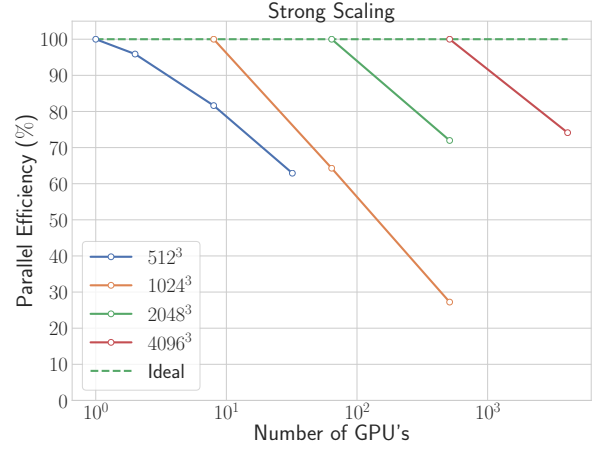
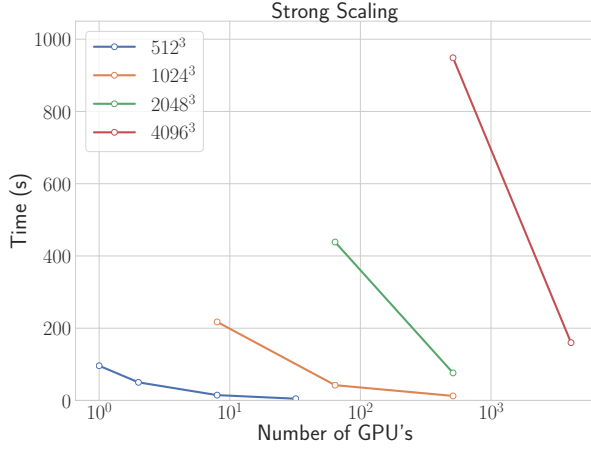


Figure 4: Performance indicators for our multiple GPU code; strong scaling is shown in the top panels, while weak scaling can be seen in the bottom ones. The Left-hand side panels show wall-clock time for a full-run (for the strong scaling plot) or the amount of wall-clock time necessary to complete 640 time-steps (for the weak scaling plot). The corresponding parallel efficiencies as defined in the text (see e.g. Eq. 19 for strong scaling) are presented on the right hand side panels.



the smallest number of GPUs (where a box of size  $N^3$  can be fitted). Speed-up is given by,

$$S = \frac{t_n}{t_{ref}}, \quad (18)$$

where  $t_n$  is the wall-clock time taken when running with  $n$  GPUs. Converted to a percentage this is trivially the parallel efficiency for weak scaling. For strong scaling the parallel efficiency is then re-scaled with the number of GPUs the reference run uses,  $n_{ref}$

$$E_{strong} = \frac{n_{ref} t_{ref}}{n t_n}. \quad (19)$$

With these defined we are in a position to describe the scalability of our application. For strong scaling there is an obvious point beyond which no useful scaling can be obtained. While we are unaware of any consensus on the definition of useful scaling, in this manuscript we assume useful scaling to only exist above 50% efficiency. Specifically, in our case this point ensues when the sub-domain size becomes too small. This is evidenced by the low parallel efficiencies seen in Table 5 and in the top panels of Figure 4 when approaching a sub-domain size of  $128^3$ . This is something relatively common in most multi-GPU implementations, at least from a cursory overview of the literature (Fuhrer et al., 2018; Potter et al., 2017).

This behaviour stems from two reasons. The first reason is the amount of communications relative to the execution of CUDA kernels: not even the overlap is sufficient for cleverly hiding this cost for extremely small sub-domains. The second reason which contributes to this behaviour is the amount of latency from launching CUDA kernels.

However disappointing the strong scaling might be, one can argue that given the relatively short run-times across the board, there isn't a need for good strong scaling. Indeed, while the largest Abelian-Higgs field theory simulations currently described in the literature have box sizes of  $4096^3$ , we have been able to carry out full (production run level)  $8192^3$  simulations, which using 4096 GPUs takes only 40.4 minutes of wall clock time. In the same  $4096^3$  GPUs, production runs of size  $4096^3$  (the largest reported in the literature so far for cosmic strings) take less than 3 minutes of wall clock time.

On the other hand, weak scaling is almost perfect up to thousands of GPUs with the lowest detected efficiency being of 91%—see Table 5 and in the bottom panels of Figure 4. This strongly suggests the overlap is being successful. Thus our code can yield production grade simulations with the largest sizes in the literature,  $4096^3$ , in between 140 and 180 node-hours (the exact number depending on the number of GPUs being used), while for  $8192^3$  simulations this increases by a factor of 16 (a factor of 8 due to the increased volume, and 2 due to the increased dynamic range) to about 2800 node-hours. Note that compute time on Piz Daint is book-kept in node-hours, and we use only one process per node. Given that it is irrelevant to use one

core or all 68 per node, one could obtain an estimate in more traditional core-hours by multiplying these numbers by a factor of 68.

To end this section we would like to comment on the usage of other metrics to assess application performance in our case. Given that, like most stencil CUDA kernels in the literature with 2.5D decomposition, our CUDA kernels end up being memory bound, we do not believe that the amount of floating point operations is a useful metric. It thus follows that we must characterize how memory bound each CUDA kernel is. This was done in the past as seen in Correia and Martins (2020) for a different GPU (specifically a QUADRO P5000 at our local cluster facility). Note however that these kernels handled the boundary conditions differently (without including ghost cells as described above). The increase of the sub-domain by two along each direction and the subsequent misaligned access do reduce the memory access bandwidth, but only impact the the overall run-time of each kernel slightly (i.e., by 2% in a worst-case-scenario).

## 6. Conclusions and outlook

We have extended our previous GPU-accelerated Abelian-Higgs string evolution code to be able to harness more than on graphical accelerator. To do so we used the Message Passing Interface to handle the necessary boundary terms of a 3D decomposed lattice. Each sub-lattice is evolved on an accelerator with the Compute Unified Device Architecture (CUDA).

In this paper we have validated the code by comparing its outcomes to those described in the literature, and also quantified its scalability. To summarize, the validation confirms a previously noticed slight decrease of the rate of change of the mean string separation as the box size is increased, while no such effect is seen in the average string velocity. A detailed study of this effect, and its possible relation to the relevant energy loss mechanisms for the cosmic strings, is left for subsequent work.

When it comes to scalability we obtain near-perfect weak scaling up to 4096 GPUs. Strong scalability is not as good, and from a comparison with the literature (Fuhrer et al., 2018) we might expect a processor only version to have a better strong scale behaviour. While this is not a limiting factor for the scientific exploitation of the code, it will be worth to explore techniques to improve this behaviour. One such possibility is the hypercube decomposition of Blanco-Pillado et al. (2012), which avoids communication and therefore achieves better scalability, and another one would be the inclusion of Mesh Refinement techniques (Drew and Shellard, 2019; Helfer et al., 2019).

It is also worthy of note that our code is not Input/Output bound when only outputting the network diagnostic quantities every few timesteps, which is the case in standard (production) runs. This changes when outputting an entire lattice of some quantity (such as the absolute value of

Box size	Number of GPU's	Domain decomposition (x,y,z)	Wall-clock time (s)	Speed-Up	Efficiency (%)
512 <sup>3</sup>	1	(1,1,1)	96.0	-	100.0
	2	(1,1,2)	50.1	1.92	95.9
	8	(2,2,2)	14.7	6.53	81.6
	32	(2,4,4)	4.77	20.12	62.9
1024 <sup>3</sup>	8	(2,2,2)	217.39	-	100.0
	64	(4,4,4)	42.27	5.14	64.2
	512	(8,8,8)	12.48	17.41	27.2
2048 <sup>3</sup>	64	(4,4,4)	438.45	-	100.0
	512	(8,8,8)	76.15	5.76	72.0
4096 <sup>3</sup>	512	(8,8,8)	948.52	-	100.0
	4096	(16,16,16)	156.96	6.04	74.3
8192 <sup>3</sup>	4096	(16,16,16)	2426.13	-	100.0

Table 2: Strong scaling measurements for different lattice sizes reported in wall clock time to fully simulate a network from start to finish. We also present the speed-up (relative to the reference measurement) and a parallel efficiency.

Box size	Number of GPU's	Domain decomposition (x,y,z)	Wall-clock time (s)	Speed-Up	Efficiency (%)
256 <sup>3</sup>	1	(1,1,1)	8.93	-	100.0
256 <sup>2</sup> × 512	2	(1,1,2)	8.95	1.00	99.7
256 × 512 <sup>2</sup>	4	(1,2,2)	8.93	1.00	99.9
512 <sup>3</sup>	8	(2,2,2)	8.94	1.00	99.8
1024 <sup>3</sup>	64	(4,4,4)	9.17	0.97	97.4
1024 <sup>2</sup> × 2048	128	(4,4,8)	9.34	0.96	95.6
1024 × 2048 <sup>2</sup>	256	(4,8,8)	9.44	0.95	94.6
2048 <sup>3</sup>	512	(8,8,8)	9.68	0.92	92.2
2048 <sup>2</sup> × 4096	1024	(8,8,16)	9.61	0.92	92.9
4096 <sup>3</sup>	4096	(16,16,16)	9.81	0.91	91.2

Table 3: Weak scaling measurements for fixed box size of 256<sup>3</sup> per domain are presented above. The wall-clock time corresponds to the time to complete 640 timesteps (the number of timesteps for a full 256<sup>3</sup> size simulation). In addition we present a speed-up as well as a parallel efficiency.

scalar field, or the windings) every few timesteps for visualization or other detailed diagnostic purposes. As such we are currently exploring in-situ visualization techniques, as previously described in Ayachit et al. (2015) in order to evade this bottleneck.

In conclusion, this new version of our Abelian-Higgs cosmic string simulation can do production runs for the largest box sizes seen in the literature ( $4096^3$ ) in very competitive amounts of node-hours, and indeed do even larger boxes ( $8192^3$ ) in reasonable amounts of node-hours. Given the excellent weak scalability, which we have demonstrated up to 4096 GPUs, the numbers are even more appealing when expressed in terms of wall clock time: less than 3 minutes for  $4096^3$ , and 40.4 minutes for  $8192^3$  simulations, using the said 4096 GPUs.

We are currently leveraging such an advantage by simulating hundreds of networks at differing expansion rates to calibrate the semi-analytical model of string evolution (Martins and Shellard, 1996, 2002), appropriately extending it to account for the correct velocity-dependencies of energy loss and curvature, as seen in Martins et al. (2016). This was done for small boxes in Correia and Martins (2019), enabling a first quantitative comparison of the relative importance of the energy loss mechanisms of the networks. Given the changes in the asymptotic quantities seen in Table 3, it will be important to re-calibrate the model for each box size we are currently able to simulate. The availability of a large sample of simulations with increased spatial resolution and dynamic range will also enable a detailed study of the amount of small-scale structure of the network itself. Both of these have obvious implications for any rigorous assessment of the observational consequences of cosmic string networks.

## Acknowledgements

This work was financed by FEDER—Fundo Europeu de Desenvolvimento Regional funds through the COMPETE 2020—Operational Programme for Competitiveness and Internationalisation (POCI), and by Portuguese funds through FCT - Fundação para a Ciência e a Tecnologia in the framework of the project POCI-01-0145-FEDER-028987. J.R.C. is supported by an FCT fellowship (grant reference SFRH/BD/130445/2017). We gratefully acknowledge the support of NVIDIA Corporation with the donation of the Quadro P5000 GPU used for this research.

We acknowledge PRACE for awarding us access to Piz Daint at CSCS, Switzerland, through Preparatory Access proposal 2010PA4610 and Project Access proposal 2019204986. Technical support from Jean Favre at CSCS is gratefully acknowledged.

## References

Abbott, B.P., et al. (LIGO Scientific, Virgo), 2018. Constraints on cosmic strings using data from the first Advanced LIGO observing run. *Phys. Rev. D* 97, 102002. doi:10.1103/PhysRevD.97.102002, arXiv:1712.01168.

Achucarro, A., Avgoustidis, A., Leite, A.M.M., Lopez-Eiguren, A., Martins, C.J.A.P., Nunes, A.S., Urrestilla, J., 2014. Evolution of semilocal string networks: Large-scale properties. *Phys. Rev. D* 89, 063503. doi:10.1103/PhysRevD.89.063503, arXiv:1312.2123.

Ade, P.A.R., et al. (Planck), 2014. Planck 2013 results. XXV. Searches for cosmic strings and other topological defects. *Astron. Astrophys.* 571, A25. doi:10.1051/0004-6361/201321621, arXiv:1303.5085.

Allen, B., Shellard, E.P.S., 1990. Cosmic string evolution: A numerical simulation. *Phys. Rev. Lett.* 64, 119–122.

Ayachit, U., Bauer, A., Geveci, B., O’Leary, P., Moreland, K., Fabian, N., Mauldin, J., 2015. Paraview catalyst: Enabling in situ data analysis and visualization, in: *Proceedings of the First Workshop on In Situ Infrastructures for Enabling Extreme-Scale Analysis and Visualization*, ACM, New York, NY, USA. pp. 25–29. URL: <http://doi.acm.org/10.1145/2828612.2828624>, doi:10.1145/2828612.2828624.

Bennett, D.P., Bouchet, F.R., 1990. High resolution simulations of cosmic string evolution. 1. network evolution. *Phys. Rev. D* 41, 2408.

Bevis, N., Hindmarsh, M., Kunz, M., Urrestilla, J., 2007. CMB power spectrum contribution from cosmic strings using field-evolution simulations of the Abelian Higgs model. *Phys. Rev. D* 75, 065015. doi:10.1103/PhysRevD.75.065015, arXiv:astro-ph/0605018.

Bevis, N., Hindmarsh, M., Kunz, M., Urrestilla, J., 2010. CMB power spectra from cosmic strings: predictions for the Planck satellite and beyond. *Phys. Rev. D* 82, 065004. doi:10.1103/PhysRevD.82.065004, arXiv:1005.2663.

Bevis, N., Saffin, P.M., 2008. Cosmic string Y-junctions: A Comparison between field theoretic and Nambu-Goto dynamics. *Phys. Rev. D* 78, 023503. doi:10.1103/PhysRevD.78.023503, arXiv:0804.0200.

Binetruy, P., Bohe, A., Caprini, C., Dufaux, J.F., 2012. Cosmological Backgrounds of Gravitational Waves and eLISA/NGO: Phase Transitions, Cosmic Strings and Other Sources. *JCAP* 1206, 027. doi:10.1088/1475-7516/2012/06/027, arXiv:1201.0983.

Blanco-Pillado, J.J., Olum, K.D., Shlaer, B., 2011. Large parallel cosmic string simulations: New results on loop production. *Phys. Rev. D* 83, 083514. doi:10.1103/PhysRevD.83.083514, arXiv:1101.5173.

Blanco-Pillado, J.J., Olum, K.D., Shlaer, B., 2012. A new parallel simulation technique. *J. Comput. Phys.* 231, 98–108. doi:10.1016/j.jcp.2011.08.029, arXiv:1011.4046.

Briggs, J., Pennycook, S.J., Shellard, E.P.S., Martins, C.J.A.P., Woodacre, M., Feind, K., 2014. Unveiling the Early Universe: Optimizing Cosmology Workloads for Intel Xeon Phi Coprocessors in an SGI UV20 00 System. Technical Report. SGI/Intel White Paper.

Correia, J., Martins, C., 2019. Extending and Calibrating the Velocity dependent One-Scale model for Cosmic Strings with One Thousand Field Theory Simulations. *Phys. Rev. D* 100, 103517. doi:10.1103/PhysRevD.100.103517, arXiv:1911.03163.

Correia, J.R.C.C.C., Martins, C.J.A.P., 2017. General purpose graphics-processing-unit implementation of cosmological domain wall network evolution. *Phys. Rev. E* 96, 043310. URL: <https://link.aps.org/doi/10.1103/PhysRevE.96.043310>, doi:10.1103/PhysRevE.96.043310.

Correia, J.R.C.C.C., Martins, C.J.A.P., 2020. Abelian-Higgs Cosmic String Evolution with CUDA. *Astronomy and Computing* 32, 100388. doi:https://doi.org/10.1016/j.ascom.2020.100388, arXiv:1809.00995.

Daverio, D., Hindmarsh, M., Kunz, M., Lizarraga, J., Urrestilla, J., 2016. Energy-momentum correlations for Abelian Higgs cosmic strings. *Phys. Rev. D* 93, 085014. doi:10.1103/PhysRevD.93.085014, arXiv:1510.05006. [Erratum: *Phys. Rev. D* 95, 049903 (2017)].

Drew, A., Shellard, E.P.S., 2019. Radiation from Global Topological Strings using Adaptive Mesh Refinement: Methodology and Massless Modes arXiv:1910.01718.

Finelli, F., et al. (CORE), 2018. Exploring cosmic origins with

- CORE: Inflation. JCAP 04, 016. doi:10.1088/1475-7516/2018/04/016, arXiv:1612.08270.
- Fuhrer, O., Chadha, T., Hoefler, T., Kwasniewski, G., Lapil-  
lonne, X., Leutwyler, D., Lüthi, D., Osuna, C., Schär, C.,  
Schulthess, T.C., Vogt, H., 2018. Near-global climate simula-  
tion at 1 km resolution: establishing a performance baseline on  
4888 gpus with cosmo 5.0. Geoscientific Model Development 11,  
1665–1681. URL: [https://www.geosci-model-dev.net/11/1665/](https://www.geosci-model-dev.net/11/1665/2018/)  
2018/, doi:10.5194/gmd-11-1665-2018.
- Helfer, T., Aurrekoetxea, J.C., Lim, E.A., 2019. Cosmic String  
Loop Collapse in Full General Relativity. Phys. Rev. D99, 104028.  
doi:10.1103/PhysRevD.99.104028, arXiv:1808.06678.
- Hindmarsh, M., Lizarraga, J., Urrestilla, J., Daverio, D., Kunz, M.,  
2017a. Scaling from gauge and scalar radiation in Abelian Higgs  
string networks. Phys. Rev. D96, 023525. doi:10.1103/PhysRevD.  
96.023525, arXiv:1703.06696.
- Hindmarsh, M., Rummukainen, K., Weir, D.J., 2017b. Numer-  
ical simulations of necklaces in SU(2) gauge-Higgs field the-  
ory. Phys. Rev. D95, 063520. doi:10.1103/PhysRevD.95.063520,  
arXiv:1611.08456.
- Kajantie, K., Karjalainen, M., Laine, M., Peisa, J., Rajantie, A.,  
1998. Thermodynamics of gauge invariant U(1) vortices from  
lattice Monte Carlo simulations. Phys. Lett. B428, 334–341.  
doi:10.1016/S0370-2693(98)00440-7, arXiv:hep-ph/9803367.
- Kibble, T.W.B., 1976. Topology of Cosmic Domains and Strings. J.  
Phys. A9, 1387–1398. doi:10.1088/0305-4470/9/8/029.
- Lopez-Eiguren, A., Lizarraga, J., Hindmarsh, M., Urrestilla, J.,  
2017a. Cosmic Microwave Background constraints for global  
strings and global monopoles. JCAP 1707, 026. doi:10.1088/  
1475-7516/2017/07/026, arXiv:1705.04154.
- Lopez-Eiguren, A., Urrestilla, J., Achúcarro, A., 2017b. Measuring  
Global Monopole Velocities, one by one. JCAP 1701, 020. doi:10.  
1088/1475-7516/2017/01/020, arXiv:1611.09628.
- Martins, C.J.A.P., 2016. Defect Evolution in Cosmology and  
Condensed Matter: Quantitative Analysis with the Velocity-  
Dependent One-Scale Model. Springer.
- Martins, C.J.A.P., Rybak, I.Y., Avgoustidis, A., Shellard, E.P.S.,  
2016. Extending the velocity-dependent one-scale model for do-  
main walls. Phys. Rev. D93, 043534. doi:10.1103/PhysRevD.93.  
043534, arXiv:1602.01322.
- Martins, C.J.A.P., Shellard, E.P.S., 1996. Quantitative string evolu-  
tion. Phys. Rev. D54, 2535–2556. doi:10.1103/PhysRevD.54.2535,  
arXiv:hep-ph/9602271.
- Martins, C.J.A.P., Shellard, E.P.S., 2002. Extending the velocity de-  
pendent one scale string evolution model. Phys. Rev. D65, 043514.  
doi:10.1103/PhysRevD.65.043514, arXiv:hep-ph/0003298.
- Martins, C.J.A.P., Shellard, E.P.S., 2006. Fractal properties and  
small-scale structure of cosmic string network s. Phys. Rev. D73,  
043515. arXiv:astro-ph/0511792.
- Moore, J.N., Shellard, E.P.S., Martins, C.J.A.P., 2002. On the evo-  
lution of Abelian-Higgs string networks. Phys. Rev. D65, 023503.  
doi:10.1103/PhysRevD.65.023503, arXiv:hep-ph/0107171.
- Olum, K.D., Vanchurin, V., 2007. Cosmic string loops in the expand-  
ing universe. Phys. Rev. D75, 063521. arXiv:astro-ph/0610419.
- Potter, D., Stadel, J., Teyssier, R., 2017. PKDGRAV3: Beyond  
Trillion Particle Cosmological Simulations for the Next Era of  
Galaxy Surveys. Computational Astrophysics and Cosmology 4,  
2. doi:10.1186/s40668-017-0021-1, arXiv:1609.08621.
- PRACE, 2017. Best practice guide gpgpu. [https://prace-ri.eu/  
wp-content/uploads/Best-Practice-Guide\\_GPGPU.pdf](https://prace-ri.eu/wp-content/uploads/Best-Practice-Guide_GPGPU.pdf).
- Press, W.H., Ryden, B.S., Spergel, D.N., 1989. Dynamical Evolution  
of Domain Walls in an Expanding Universe. Astrophys. J. 347,  
590–604. doi:10.1086/168151.
- Wilson, K.G., 1974. Confinement of quarks. Phys. Rev. D 10, 2445–  
2459. URL: [https://link.aps.org/doi/10.1103/PhysRevD.10.](https://link.aps.org/doi/10.1103/PhysRevD.10.2445)  
2445, doi:10.1103/PhysRevD.10.2445.